ADVANCED MATERIALS
www.advmat.de

Uncovering the Intrinsic High Fracture Toughness of Titanium via Lowered Oxygen Impurity Content

Xiao-Wei Zou, Wei-Zhong Han, and En Ma**

Titanium (Ti) and its alloys are known to exhibit room-temperature fracture toughness below 130 MPa $m^{1/2}$, only about one half of the best austenitic stainless steels. It is purported that this is not the best possible fracture resistance of Ti, but a result of oxygen impurities that sensitively retard the activities of plasticity carriers in this hexagonal close-packed metal. By a reduction of oxygen content from the 0.14 wt% in commercial purity Ti to 0.02 wt%, the mode-I fracture toughness of the low-oxygen Ti is measured to be as high as $K_{J_{Ic}} \approx 255$ MPa $m^{1/2}$, corresponding to *J*-integral-based crack-initiation toughness of up to $J_{Ic} \approx 537$ kJ m^{-2}. This extraordinary toughness, reported here for the first time for pure Ti, places Ti among the toughest known materials. The intrinsic high fracture resistance is attributed to the profuse plastic deformation in a significantly enlarged plastic zone, rendered by the pronounced deformation twinning ahead of the crack tip along with ample twin-stimulated ⟨*c*+*a*⟩ dislocation activities, in the absence of impeding oxygen. Controlling the content of a property-controlling impurity thus holds the promise to be a readily applicable strategy to reach for unprecedented damage tolerance in some other structural alloys.

1. Introduction

Titanium (Ti) is an attractive material across a wide range of areas, widely used in aerospace, military, automotive, medical implants, sporting goods, jewelry, mobile phones, corrosive environments, and other applications.[1–3] With regard to mechanical properties, Ti is a strong yet ductile metal with low density, recognized for its highest strength-to-weight ratio of any metallic element.[4–7] However, the damage tolerance, i.e., resistance to fracture, is not a forte of Ti; the fracture toughness of Ti, despite decades of efforts improving processing and introducing alloying elements, has always been limited to below 130 MPa $m^{1/2}$ – notably lower than the toughest metallic materials such as some austenitic stainless steels and medium/high entropy alloy (M/HEAs), which boast fracture toughness exceeding 200 MPa $m^{1/2}$.[8–16] This shortfall in fracture resistance hampers the application of Ti under certain safety critical loading conditions. An important question naturally arises: is the fracture toughness observed so far already the best-case scenario intrinsic to this metal, and would it ever be possible for Ti to exhibit a fracture toughness that rivals the toughest metals?

To answer this question, we first note that the fracture resistance of a material depends on its inherent mechanisms that can be activated to make crack propagation difficult.[17,18] This is usually gauged by the plastic flow ahead of the crack tip; the larger the plastic process zone, the higher the fracture toughness.[17] Unfortunately, compared to readily deformable face-centered-cubic (FCC) metals, the hexagonal closed-packed (HCP) crystal structure of α-Ti is of lower symmetry with obvious anisotropy, which usually leads to limited uniform deformation due to a small number of slip systems.[19–27] The primary dislocation slip mode in HCP Ti is prismatic ⟨*a*⟩ slip as it exhibits the lowest critical resolved shear stress (CRSS).[24,25] However, this slip system alone cannot accommodate the ⟨*c*⟩-axis strain and satisfy the von Mises criterion.[19–27] To achieve more uniform deformation, additional deformation mechanisms along the ⟨*c*⟩-axis such as pyramidal ⟨*c*+*a*⟩ slip and deformation twinning become imperative.[20,23] Unfortunately, these mechanisms are usually inactive due to their much higher CRSS compared to prismatic ⟨*a*⟩ slip.[24,25]

This predicament, we propose, is largely due to the oxygen impurities in commercial purity Ti (CP-Ti, with oxygen content of 0.14 wt%),[28–33] as twinning and dislocation activities in Ti can be adversely and sensitively affected by oxygen solutes during both uniaxial tensile and impact deformation, even when their contents are rather low.[29,34] In what follows, we demonstrate that a simple reduction of the content of oxygen (by a factor of 7–0.022 wt%; hereafter referred to as low-oxygen Ti, LO-Ti) can dramatically promote deformation twinning ahead of the crack tip in Ti, and the twinning in turn stimulates ample ⟨*c*+*a*⟩ dislocation activities. These mechanisms collectively promote the ⟨*c*⟩-axis deformation. As a result of this drastically increased plastic flow and

X.-W. Zou, W.-Z. Han
Center for Advancing Materials Performance from the Nanoscale, State Key Laboratory for Mechanical Behaviour of Materials
Xi'an Jiaotong University
Xi'an 710049, P. R. China
E-mail: wzhanxjtu@mail.xjtu.edu.cn
E. Ma
Center for Alloy Innovation and Design, State Key Laboratory for Mechanical Behavior of Materials
Xi'an Jiaotong University
Xi'an 710049, P. R. China
E-mail: maen@xjtu.edu.cn
The ORCID identification number(s) for the author(s) of this article can be found under https://doi.org/10.1002/adma.202408286

DOI: 10.1002/adma.202408286

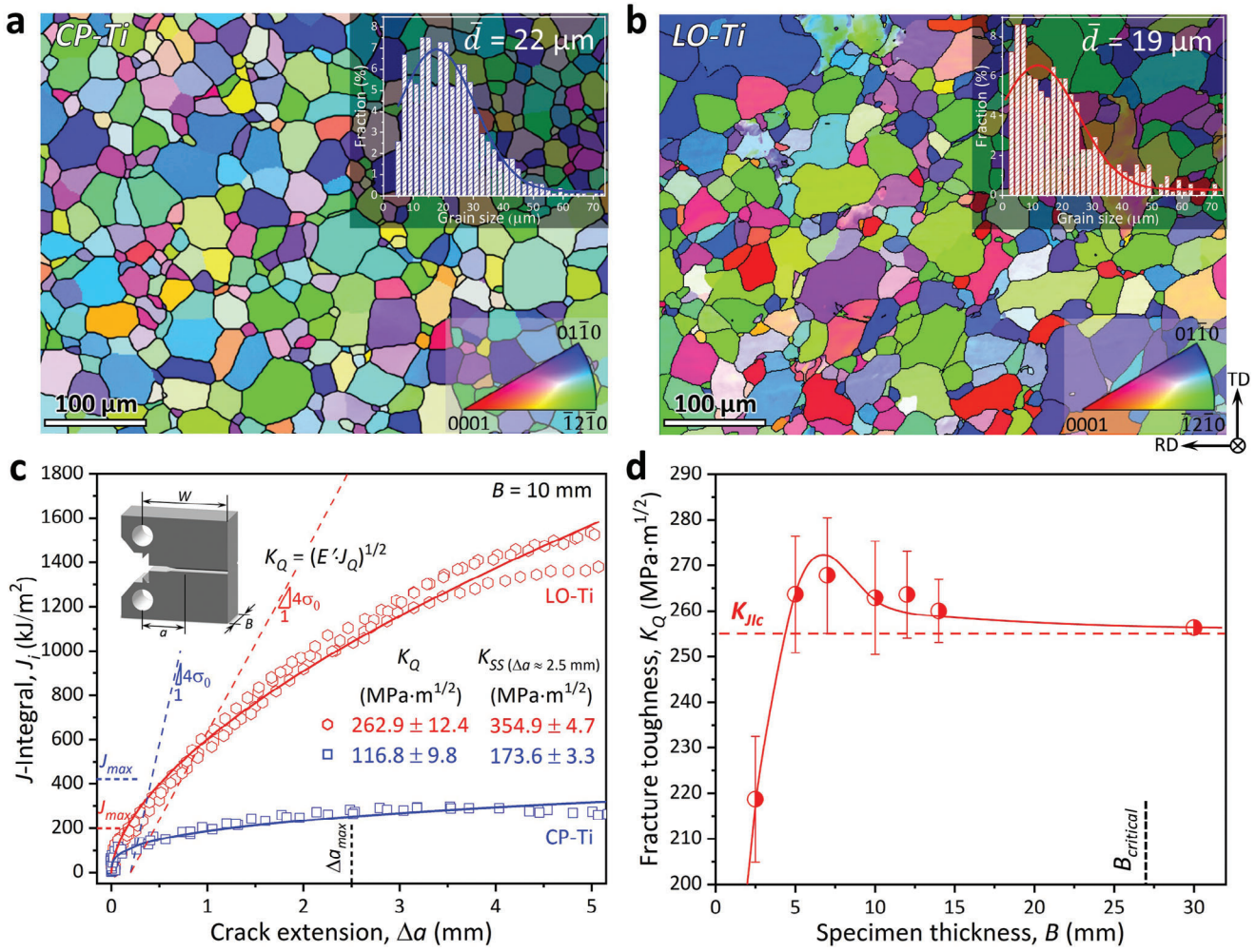

Figure 1. Microstructure and fracture toughness of the commercial pure Ti (CP-Ti) and low-oxygen Ti (LO-Ti). a,b) EBSD scans show similarly sized equiaxed grains in a) CP-Ti and b) LO-Ti. The sample direction associated with the IPF coloring is the direction normal to the EBSD scan plane. c) The *J*-integral-based resistance curves (*J*–*R* curves) measured from the compact tension (CT) specimens with thickness $B = 10$ mm and width $W = 20$ mm at room temperature. According to ASTM E1820 standard,[35] a power law, $J = C_1(\Delta a)^{C2}$, is adopted to fit the data; see the solid lines. The *K*-based fracture toughness K_Q values for the CP-Ti and LO-Ti are 116.8 and 262.9 MPa m$^{1/2}$, respectively. d) The measured toughness with respect to specimen thickness, *B*. The fracture toughness converges to a stable value ≈255 MPa m$^{1/2}$, when *B* approaches and exceeds $B_{critical} = 10J_{Ic}/\sigma_0 = 27$ mm.

uniform deformation capacity ahead of the crack tip, the intrinsic high fracture resistance of Ti is brought out for the first time. The fracture toughness of LO-Ti exceeds by far that of all previously reported commercial purity grade Ti and its alloys and in fact surpasses almost all known metallic materials. Such a strategy to judiciously diminish the content of minor impurity elements offers a promising direction for the design of high-toughness Ti alloys.

2. Results and Discussion

2.1. Microstructure and Fracture Resistance

The pure Ti we used was low-oxygen Ti with oxygen content (0.022 wt%), a factor of 7 lower compared with CP-Ti (0.14 wt% oxygen). The detailed chemical compositions are listed in Table S1 (Supporting Information). Both the LO-Ti and CP-Ti specimens were rolled to 30% thickness reduction at room temperature, followed by recrystallization annealing at 700 °C for 0.5 h to obtain an equiaxed grain structure. For the two types of Ti, we characterized their uniaxial tensile properties, measured their fracture toughness using the compact-tension (CT) specimens in accordance with ASTM E1820,[35] and evaluated their impact energy using Charpy V-notch samples following ASTM E23.[36] All mechanical tests were conducted at room temperature.

Figure 1a,b displays the electron backscattered diffraction (EBSD) microscopic images for the fully recrystallized microstructure of LO-Ti and CP-Ti specimens, respectively. The average grain sizes of the two Ti samples are comparable: ≈19 μm for LO-Ti and ≈22 μm for CP-Ti. EBSD pole figures indicate that the ⟨*c*⟩-axis of many grains in CP-Ti and LO-Ti samples exhibits a preferential alignment to a small degree toward the transverse direction (TD) and the normal direction (ND) of the rolled plates, respectively (Figure S1, Supporting Information). The engineering stress–strain curves, measured in uniaxial tension, are shown

in Figure S2a (Supporting Information). LO-Ti shows a lower strength (yield strength $\sigma_y \approx 142$ MPa) compared with CP-Ti ($\sigma_y \approx$ 340 MPa), but much higher tensile ductility with a uniform elongation exceeding 35% (see details in Table S2 in the Supporting Information). Both the CP-Ti and LO-Ti show strong strain hardening ability, with strain-hardening exponent values of $n \approx 0.49$ and $n \approx 0.38$, respectively; see Figure S2b,c (Supporting Information). Notably, during the stage of uniform deformation, CP-Ti exhibits minimal deformation twins, whereas LO-Ti generates more twins, indicating that dislocation slipping is the predominant plastic deformation mode in CP-Ti. Triaxial stress during necking promotes the activation of deformation twins in both CP-Ti and LO-Ti, as shown in Figure S3 (Supporting Information). Therefore, prior to necking, the presence of trace oxygen atoms in Ti significantly enhances its strain hardening rate by effectively pinning and storing dislocations. In contrast, Ti with low oxygen may experience a weaker trapping effect on dislocations, and shows relatively less dislocation accumulation and lower strain hardening rate.

In view of the extensive plastic deformation capacity of Ti, the fracture resistance was evaluated based on nonlinear elastic fracture mechanics, employing J-integral-based crack-resistance R-curves (J as a function of the stable crack extension, Δa). The J-integral value of crack initiation (J_Q) was determined by the intersection point of J–Δa curves and the 0.2 mm offset line,[35] $J = M\sigma_0\Delta a$, where $M = 2$ or 4, and σ_0 is the effective yield strength, $\sigma_0 = (\sigma_y + \sigma_{uts})/2$, σ_{uts} is the ultimate tensile strength. For high strain-hardening materials with low strength (σ_y below 400 MPa and strain-hardening exponent n greater than 0.2),[37] setting the M value to 4 can appropriately reflect the blunting effect at the crack tip. As shown by the true stress–true strain curves in Figure S2 (Supporting Information), both Ti samples exhibit low yield strength and a fairly high strain-hardening exponent, thus $M = 4$ is appropriate here (the fracture toughness value would be even higher if we chose $M = 2$). We then back-calculated the corresponding stress intensity-based fracture toughness value K_Q from the J_Q value (Figure 1c) according to $K = (E' \times J_Q)^{1/2}$, where $E' = E$ (Young's modulus) in plane stress and $E/(1 - \nu^2)$ (where ν is the Poisson's ratio) in plane strain. Both types of Ti, especially LO-Ti, display rising R-curves. LO-Ti with a thickness of $B = 10$ mm and a width of $W = 20$ mm exhibits an exceedingly high average crack-initiation toughness value of $K_Q \approx 262.9$ MPa m$^{1/2}$, which is more than twice that of CP-Ti with the same thickness ($K_Q = 116.8$ MPa m$^{1/2}$).

According to ASTM E1820,[35] the provisional toughness K_Q obtained from LO-Ti with $B = 10$ mm could be sample size dependent as the sample dimensions did not meet the plane-strain condition (which requires $B > 27$ mm; see the Supplementary Text in the Supporting Information). Therefore, to meet the specific validity criteria outlined in ASTM E1820,[35] we extended the measurements of J–R curves to LO-Ti samples with a wide range of thicknesses, from 2.5 mm all the way to 30 mm (beyond the critical thickness; Figures S3 and S4, Supporting Information). As shown in Figure 1d, the K_Q is found to converge to a stable value of $\approx$ 255 MPa m$^{1/2}$, which may then be taken as the ASTM-valid fracture toughness (K_{JIc}) under J-field dominance and plane-strain conditions (see the Supplementary Text in the Supporting Information). The negligible necking for $B = 30$ mm further supports the validity of K_{JIc} value under plane strain conditions (Figure S5d, Supporting Information). In addition, with the yield strength of LO-Ti ($\approx$142 MPa) reduced to about half that of CP-Ti ($\approx$340 MPa), which increases the plastic dissipation that occurs at the crack tip, the J-integral-based fracture toughness ($J_{Ic} \approx 537$ kJ m^{-2}) rises to five times that of CP-Ti ($\approx$113 kJ m^{-2}), exhibiting a remarkable increase in fracture energy. The K_{JIc} value of LO-Ti at room temperature was an exceptionally high crack-initiation toughness not observed in any other Ti and its alloys (always below 130 MPa m$^{1/2}$).[8–11] In other words, the reduced oxygen enables a direct observation of the intrinsic high fracture toughness of Ti.

The impact energy of LO-Ti was measured to be 279 J, which is three times that of the CP-Ti counterpart (87 J) (Figure S6, Supporting Information); another recent and separate impact test confirmed this result.[34] This comparison, via standard Charpy impact test, further demonstrates the remarkable fracture resistance of LO-Ti, well beyond that of CP-Ti.

2.2. Fracture Behavior and Failure Mechanisms

To understand the toughening mechanisms responsible for the exceptional crack propagation resistance of LO-Ti, we characterized and compared the fracture behaviors of CP-Ti and LO-Ti CT samples. The fracture surfaces of the two CT samples were analyzed using a scanning electron microscope (SEM). The difference in fracture toughness value measured between the LO-Ti CT sample with $B = 10$ mm ($K_{JIc} = 262.9$ MPa m$^{1/2}$) and $B = 30$ mm ($K_{JIc} = 256.3$ MPa m$^{1/2}$) is within 3%, suggesting similar fracture and failure mechanisms for both samples. Therefore, we select the CT sample with $B = 10$ mm to characterize the deformation morphologies for LO-Ti under near-plane-strain conditions. Some samples with $B = 10$ mm were additionally sliced in two halves, and the resultant cross sections were polished for SEM and EBSD analysis of the region in the vicinity of the crack tip. The fracture surfaces of CP-Ti sample showed semibrittle fracture characteristics with quasi-cleavage fracture mode (**Figure** 2a,b), whereas LO-Ti exhibited fully ductile failure by microvoid coalescence, with dimple sizes in the range of tens of micrometers (Figure 2e,f). At the midthickness surface, although CP-Ti showed slightly deflected crack path (Figure S9a, Supporting Information), acting to reduce the local crack-driving force at the crack tip and contribute to the rising R-curve,[38] the crack tip is sharp and the crack tip opening displacement (CTOD) is small at the crack extension $\Delta a \approx 4$ mm under near-plane-strain condition (Figure S9a, Supporting Information). In contrast, LO-Ti exhibited much larger CTOD compared to CP-Ti and the crack tip was significantly blunted at the same crack extension (Figure 2g; Figure S9b, Supporting Information). Based on the J–CTOD equivalence relationship, $J \propto \sigma_0$CTOD,[12] the CTOD of LO-Ti being much larger than that of CP-Ti accounts for the major part of the striking jump in J-integral fracture toughness of LO-Ti, which has a lower flow stress σ_0.

EBSD band contrast (BC) and inverse pole figure (IPF) maps of LO-Ti (Figure 2g,h) reveal profuse deformation twinning within the plastic zone near the crack profile and in the vicinity of the crack tip, in contrast to CP-Ti (Figure 2c,d), both examined at the same crack extension of 4 mm. Furthermore, the number of grains generating twins in LO-Ti is significantly higher than

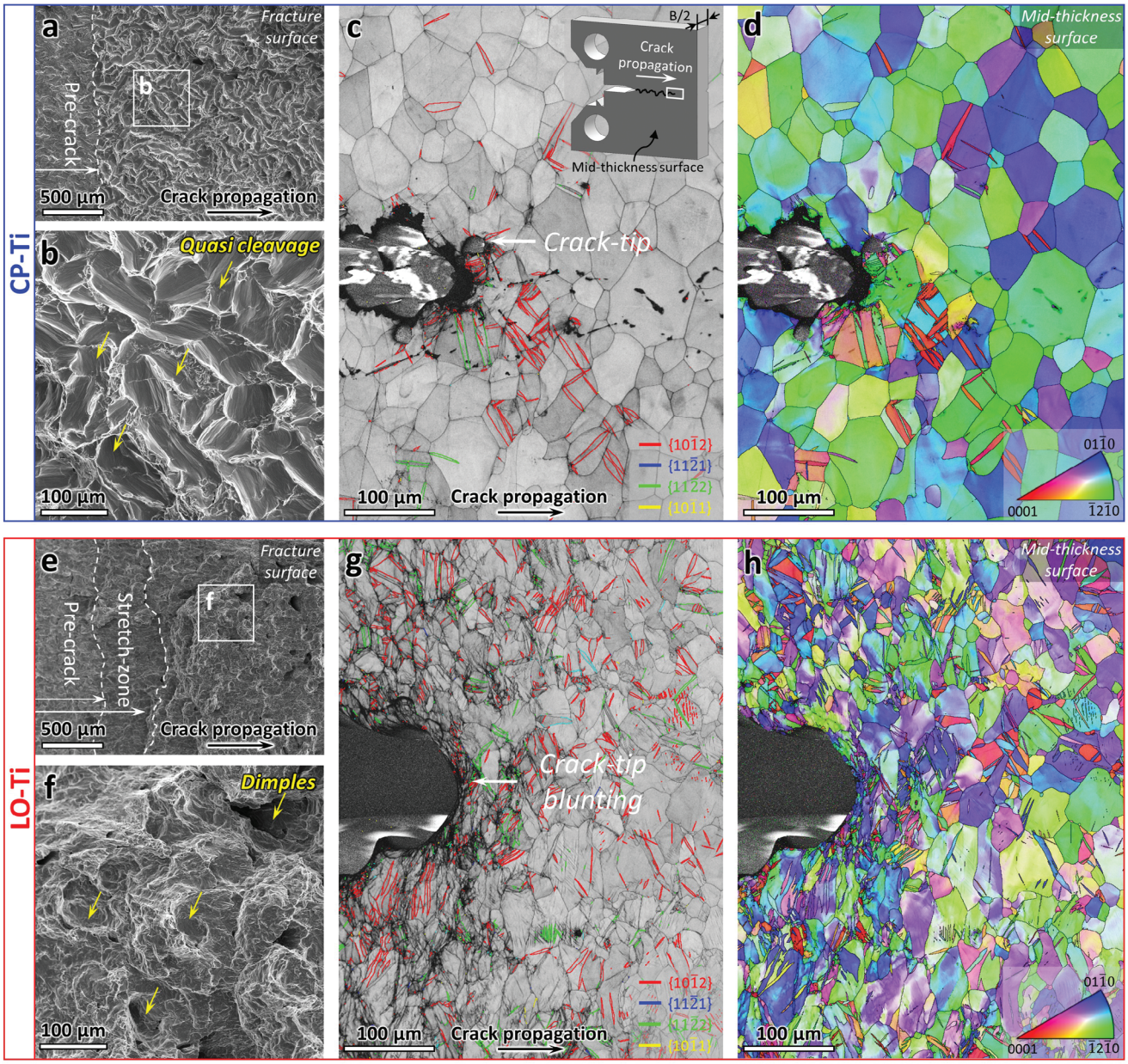

Figure 2. Fracture behaviors of the CP-Ti and LO-Ti CT samples (B = 10 mm). a,b) The fracture surfaces of CP-Ti show the quasi-cleavage fracture mode, whereas e,f) LO-Ti exhibits obviously ductile fractures with lots of dimples. EBSD maps of c,d) CP-Ti and g,h) LO-Ti show the microstructures in the heavily deformed region directly near the crack profile and ahead of the crack tip (within the plastic zone). A much larger number of deformation twins (marked red and green) are observed in the LO-Ti than in the CP-Ti case, making a significant contribution to the blunting of crack tip in panel (g).

that in CP-Ti (Figure 2; Figure S9c–h, Supporting Information). Numerous twin boundaries (TBs) within grains in LO-Ti divide each grain into multiple regions, resulting in grain refinement near the crack tip (Figure 2h; Figure S10, Supporting Information). This TB-induced grain refinement is nearly nonexistent in CP-Ti due to the limited number of TBs. The continuous activation of multiple twin variants, as seen in Figure 2g, is also expected to promote uniform deformation ahead of the crack tip.[5,39] Superior fracture toughness has also been achieved in other metals, when a high density of deformation twins is produced ahead of the crack tip, especially at cryogenic temperature, such as in some austenitic stainless steels and M/HEAs.[12–16] Additionally, after tensile testing, both CP-Ti and LO-Ti show a ductile fracture surface with numerous dimples. However, the dimples in LO-Ti are notably denser compared to CP-Ti. Particularly, a significantly greater number of thinner elongated deformation twins are observed after necking in LO-Ti, accompanied by numerous microvoids nucleated along twin boundaries (Figure S3h–j, Supporting Information). Therefore, we believe that the profuse deformation twinning not only enhances the plastic activity at the crack tip in the LO-Ti sample, but may also affect the damage mechanism, which requires further work. Importantly,

these deformation twins provide the necessary path to accommodate deformation along the ⟨*c*⟩-axis for HCP metals.[19] To date, there have been four common deformation twinning modes reported for Ti, including two tension twins ($T1\{10\bar{1}2\}\langle\bar{1}011\rangle$ and $T2\{\bar{1}\bar{1}21\}\langle11\bar{2}\bar{6}\rangle$) and two compression twins ($C1\{11\bar{2}2\}\langle11\bar{2}\bar{3}\rangle$ and $C2\{10\bar{1}1\}\langle10\bar{1}\bar{2}\rangle$).[29] The types of deformation twins in LO-Ti were confirmed to be mainly $\{10\bar{1}2\}$ (in red color in Figure 2g) and $\{11\bar{2}2\}$ twins (in green color). Apparently, the small amount of oxygen in CP-Ti has the effect of inhibiting deformation twinning activity at the crack tip. Previous studies of the interaction between the oxygen and TBs had shown that oxygen solutes tend to segregate at the $\{10\bar{1}2\}$ TBs and impede the shearing motion of atomic planes during twinning, resulting in the pinning and slower migration of TBs.[28,29] Therefore, our LO-Ti effectively eliminates the inhibition effect caused by oxygen. The activation of massive deformation twinning opens a new avenue toward an extraordinarily large plastic zone at the crack tip in LO-Ti, which is augmented by profuse dislocation activities not present in CP-Ti, as will be emphasized next.

2.3. Enhanced ⟨*c*+*a*⟩ Slip Activity Ahead of the Crack Tip

The change in toughening mechanisms caused by the reduction of oxygen content is also reflected by the morphology and density of dislocations ahead of the crack tip in CP-Ti and LO-Ti CT specimens. We used a transmission electron microscope (TEM) to characterize the dislocation structures near the crack tip, and the types of the dislocations were determined by using the standard **g**•**b** analysis (where **g** is the diffraction vector and **b** is the Burgers vector of dislocations). In CP-Ti, the majority of dislocations in the matrix were of ⟨*a*⟩-type with $b = 1/3\langle11\bar{2}0\rangle$; this is supported by the observation that most visible dislocations under $\mathbf{g} = \bar{1}100$ in **Figure** 3a are invisible under $\mathbf{g} = 0002$ in Figure 3b within the same region. Some ⟨*c*+*a*⟩ types with $\mathbf{b} = 1/3\langle11\bar{2}3\rangle$ were detected inside the *T*1 twin under the [0002] reflection (Figure 3c). It is worth noting that a few ⟨*c*+*a*⟩ dislocations inside matrix slipped in planar slip mode (Figure S12a, Supporting Information), which is further confirmed by the morphology of planar slip bands near the crack tip on the surface of the CP-Ti CT sample (Figure S8a–f, Supporting Information). In Ti—O alloys, the shuffling of oxygen has been proposed to explain the planar slip of ⟨*a*⟩ dislocations.[29,30] This mechanism may also promote the planar slip of ⟨*c*+*a*⟩ dislocations. In addition, the pyramidal ⟨*c*+*a*⟩ dislocations in CP-Ti sample have a tendency to straighten in the direction corresponding to the intersection line of the pyramidal glide plane with the basal plane (Figure S12b, Supporting Information). This alignment indicates that these ⟨*c*+*a*⟩ dislocations possess a large edge component with a character angle of 105° (slipping on the first-order pyramidal plane) or 90° (slipping on the second-order pyramidal plane) between the Burgers vector and dislocation line (Figure S12b, Supporting Information), which are known to have a low mobility.[22,40,41] The discrepancy in the mobility of edge and screw component of the ⟨*c*+*a*⟩ dislocations might affect its self-multiplication efficiency.[42]

In LO-Ti, the dislocation structures ahead of the crack tip are substantially different, as illustrated in Figure 3f–j and Figure S12c,d (Supporting Information). A high density of dislocations has been activated in the matrix (Figure 3f,g). Although it is difficult to distinguish the dislocation type in Figure 3f because both ⟨*a*⟩-type and ⟨*c*+*a*⟩-type are visible under $\mathbf{g} = \bar{1}100$, ⟨*a*⟩ slip is still inferred to be significantly activated due to its low CRSS.[24,25] In addition, the high average geometrically necessary dislocation (GND) density (Figure S11h, Supporting Information) demonstrates the activation of ample ⟨*a*⟩ dislocations, leading to pronounced plastic deformation along the ⟨*a*⟩-axis. However, the ⟨*a*⟩ dislocation motion alone would not be sufficient to accommodate an arbitrary plastic deformation at the crack tip.[31,43] This dilemma is resolved through deformation twinning, and importantly the ensuing activation of ample ⟨*c*+*a*⟩ dislocations that provide an additional mechanism for accommodating the deformation along the ⟨*c*⟩-axis.[19–27] Generally, ⟨*c*+*a*⟩ dislocations in Ti and its alloys are few and far between because of the much higher CRSS of ⟨*c*+*a*⟩ slip,[24,25] except under specific conditions such as deformation along the ⟨*c*⟩-axis or at high temperatures.[2] This is no longer the case in the LO-Ti sample, where ⟨*c*+*a*⟩ dislocations ahead of the crack tip increased significantly in density. This behavior was observed in both the matrix (Figure 3g) and inside the twins (Figure 3h). Multiple mechanisms may in fact be responsible for the activation of profuse ⟨*c*+*a*⟩ dislocations ahead of the crack tip. First, the reduction in oxygen content in LO-Ti lowers the CRSS for the activation of ⟨*c*+*a*⟩ slip;[39] second, the triaxial tensile stress state under plane-strain conditions and high stress concentration near the crack tip make it easier to reach the CRSS for ⟨*c*+*a*⟩ slip;[18] third, high-density TBs serve as sources for the emission of a large number of ⟨*c*+*a*⟩ dislocations into both the matrix and twins; the source-like behavior is evidenced by the "bow-out" shape of the ⟨*c*+*a*⟩ dislocations at the TBs; see Figure 3i,j. Indeed, high-resolution atomic images of the $\{10\bar{1}2\}$ and $\{11\bar{2}2\}$ TBs have revealed the presence of numerous small facets, which are the likely dislocation source locations due to local stress concentrations at these atomic-scale steps.[44,45] Notably, in the matrix of LO-Ti sample, there are still some ⟨*c*+*a*⟩ edge dislocations parallel to the basal plane with low mobility similar to those in CP-Ti (Figure 3g; Figure S12b, Supporting Information).[22,40,41] The decrease in dislocation self-multiplication efficiency, resulting from the difference in mobility between the edge and screw components,[42] can also be improving by providing numerous twin boundaries as dislocation sources, eventually enhancing the activity of ⟨*c*+*a*⟩ dislocations.

2.4. Ultralarge Plastic Deformation Zone at the Crack Tip

In general, the intrinsic fracture toughness of metals is primarily improved by increasing the plastic zone size, which indicates the extent of plastic deformation occurring ahead of the crack tip.[17] To visually illustrate the difference in plastic zone between the CP-Ti and LO-Ti CT samples, we captured in situ videos of the plastic zone ahead of the crack tip during crack propagation on the sample surface (Movies S1 and S2, Supporting Information). The plastic zone evolution was monitored by observing the change of brightness resulting from plastic deformation. The size of plastic zone ahead of the crack tip in LO-Ti sample (from ≈5.5 to 12.2 mm in height) is significantly larger than that of the CP-Ti (from ≈2.6 to 4.4 mm in height) whether at crack initiation (Figure S7a, Supporting Information) or at a specific crack

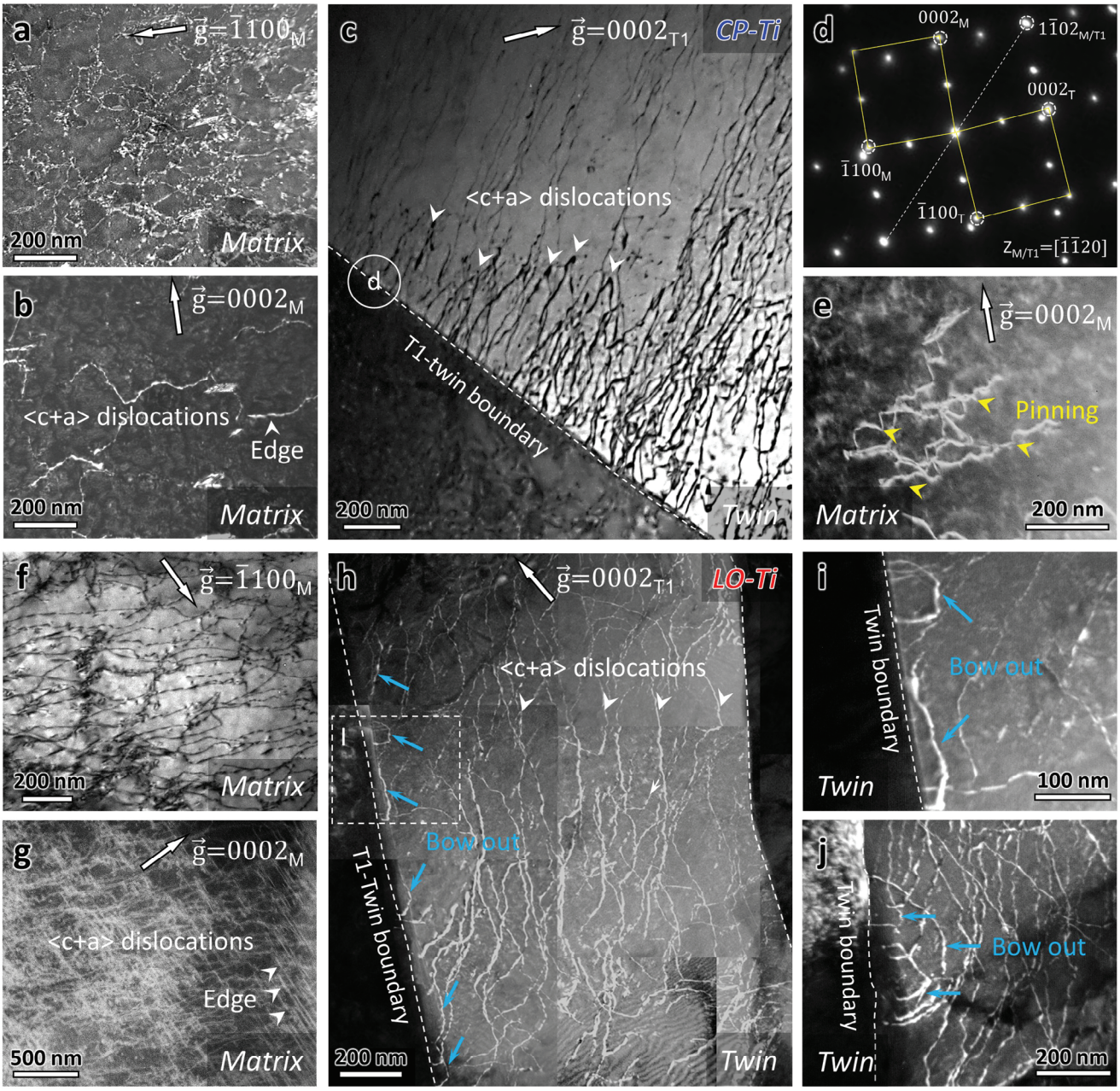

Figure 3. Deformation mechanisms ahead of the crack tip (within the plastic zone) in CP-Ti and LO-Ti CT samples (B = 10 mm). a,b) Two-beam condition analysis in CP-Ti shows that ⟨a⟩ dislocations dominate in the matrix ahead of the crack tip. c) More ⟨c+a⟩ dislocations are activated near the twin boundary. d) Selected area diffraction patterns (SADPs) showing the twin in panel (c) is {10$\bar{1}$2} twin. e) A few ⟨c+a⟩ dislocations are pinned. f,g) LO-Ti shows a high density of dislocations, especially ample ⟨c+a⟩ dislocations, in the matrix. h–j) TEM dark-field images show a large number of ⟨c+a⟩ dislocations with bow-out shapes near a twin boundary inside the {10$\bar{1}$2} twins. Twin boundaries in LO-Ti appear to be efficient source for ⟨c+a⟩ dislocation.

extension (Figure S7b, Supporting Information) under plane stress conditions. It is worth highlighting that the crack tip exhibited clear blunting during crack initiation in LO-Ti, whereas in the CP-Ti sample, the crack tip was always sharp and propagated rapidly (Figure S7a, Supporting Information). This observation is consistent with the much higher crack-initiation toughness of LO-Ti. The kernel average misorientation (KAM) maps and GND maps were also examined (Figure S11, Supporting Information) near the crack tip at the mid-thickness surface of CP-Ti and LO-Ti, in order to qualitatively compare the contributions of plastic deformation zone by comparing the distribution and extent of KAM (an indicator of plastic deformation) and GND density under near-plane-strain conditions.[31] In the LO-Ti CT sample, the high KAM values and GND density spread over a wider range around the crack tip, and distribute more homogeneously inside the grains, as opposed to being localized near a few grain

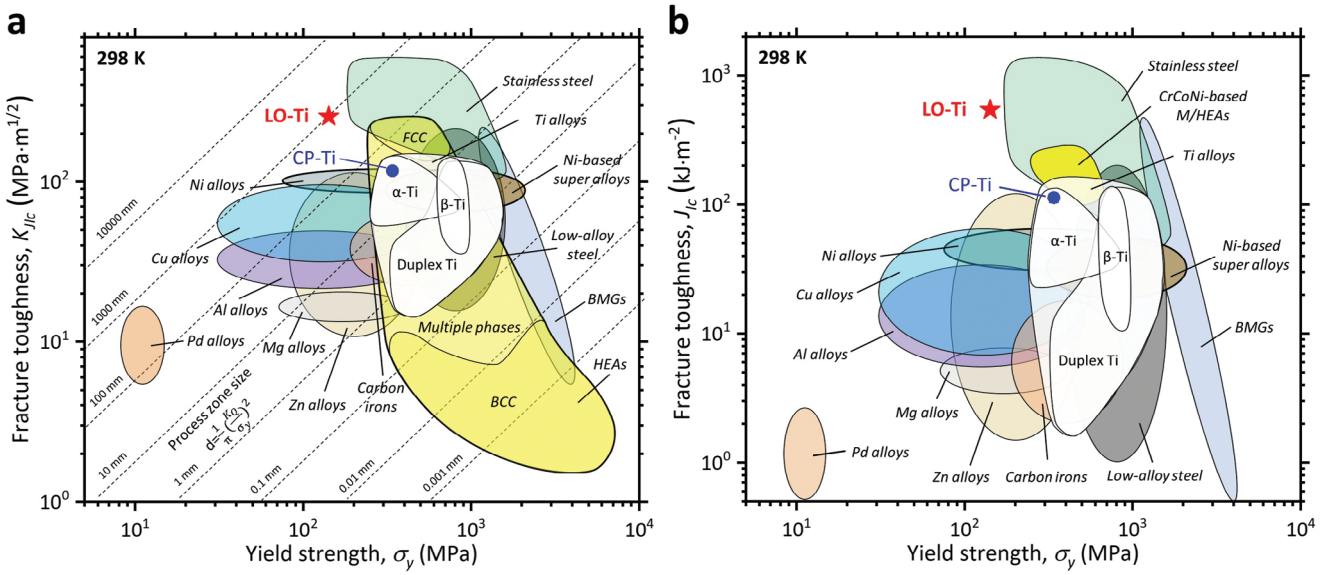

Figure 4. Ashby map of fracture toughness versus yield strength for a wide range of metals at room temperature. b) The J_{Ic} values of different metals are backcalculated from K_{JIc} in panel (a) according to $J_{Ic} = K_{JIc}^2 \times (1 - \nu^2)/E$. The LO-Ti shows an exceptional fracture toughness exceeding that of almost all pure metals and metallic alloys.[8–16]

boundaries at the crack tip commonly observed in the CP-Ti. This is another indication of the much larger plastic zone in LO-Ti, which promotes crack-tip blunting by releasing the localized strain at the crack tip.

We believe that the previously reported fracture toughness of Ti and its alloys is largely limited by extrinsic effects imparted by the oxygen solutes,[29–32] which are adverse with regard to plasticity mechanisms that deter crack propagation. We have found a straightforward way to unveil the intrinsic high fracture resistance of Ti. This is done via a simple reduction of the oxygen content (by a factor of 7) with respect to CP-Ti. The LO-Ti exhibits a strictly valid crack-initiation toughness of K_{JIc} exceeding 255 MPa m$^{1/2}$ at ambient temperature. To see how the LO-Ti compares with other metallic materials, the Ashby maps in **Figure 4** plot the crack-initiation fracture toughness K_{JIc} and the corresponding J_{Ic} versus yield strength σ_y at ambient temperature.[8–16] The room-temperature fracture toughness K_{JIc} of LO-Ti doubles that of CP-Ti under identical testing conditions, and exceeds that of most other metals and metallic alloys,[8–16] including single FCC-phase CrCoNi-based M/HEAs that boast high damage tolerance,[12–15] the only exception being just a couple of 316-type austenitic stainless steels,[15,16] which in most recent reports showed exceptional toughness that has markedly lifted upward the upper boundary of the stainless steel region in Figure 4. In addition, the *J*-integral-based crack-initiation toughness of our LO-Ti is much higher (J_{Ic} ≈ 537 kJ m^{-2}) even compared to CrCoNi MEAs that showed increased toughness at 77 K (J_{Ic} ≈ 363 kJ m^{-2});[13] only when the temperature drops to 20 K does their J_{Ic} (≈802 kJ m^{-2}) exceeds that of the LO-Ti.[14] Again, the high fracture toughness of LO-Ti originates from the profuse deformation twinning driven by the triaxial stresses at the crack tip, along with twin-stimulated ample ⟨*c*+*a*⟩ slip.[44,45] In particular, these activities contributed to large and uniform plastic deformation,[45–47] which tends to improve the fracture toughness of the material.

Reduced content of interstitial atoms, particularly oxygen, has been employed in certain Ti alloys with lamellar or basketweave structures to improve their fracture toughness. These Ti alloys, such as extra-low interstitial (ELI) grade Ti-6Al-4V alloy, also known as damage-tolerant Ti-6Al-4 V (TC4 DT) alloy, have been successfully developed and widely adopted in commercial applications. However, their fracture toughness remains below 130 MPa m$^{1/2}$ due to their relatively high oxygen content (<0.13 wt%).[10] Further reduction in the oxygen content may therefore significantly enhance their fracture toughness by promoting plastic deformation within the *α*-Ti phase at the crack tip.

3. Conclusion

In summary, it is the low-oxygen solute content that enabled a synergy combining ample deformation twinning and twinning-stimulated ⟨*c*+*a*⟩ dislocation slip, the two desirable deformation modes along the ⟨*c* ⟩-axis. This has facilitated uniform plastic deformation and produced an unusually large plastic zone at the crack tip, leading to an unprecedented level of fracture resistance for Ti. Intrinsically, Ti is in fact one of the toughest materials ever reported across all material classes. This is good news for the utility of Ti in damage-prone scenarios, as the LO-Ti is readily accessible on the market, with no demanding metallurgy/processing required for its availability. In addition, our success with reducing the critical-impurity content in Ti highlights a generally useful strategy to uncover the full potential of metals/alloys in their fracture resistance.

4. Experimental Section

Sample Preparation: The CP-Ti (grade TA1) and LO-Ti (4 N high-purity Ti) purchased for this study were readily available from vendors on the market (Baoji Ying Titanium Metal Materials Co., Ltd.). No additional

deoxygenation treatment was conducted for the LO-Ti before mechanical tests. Both the CP-Ti and LO-Ti samples were processed by rolling to 30% thickness reduction at ambient temperature, followed by recrystallization annealing at 700 °C for 0.5 h, to obtain a fully recrystallized microstructure. All heat treatments were carried out under an ultrahigh vacuum condition ($<1 \times 10^{-4}$ Pa) to protect against oxygen intake as much as possible. The chemical compositions of CP-Ti and LO-Ti after rolling and heat treatment are presented in Table S1 (Supporting Information). The oxygen content was measured using LECO ONH836 oxygen/nitrogen/hydrogen elemental analyzer.

Mechanical Properties Test: To characterize the uniaxial tensile properties of CP-Ti and LO-Ti, dog-bone-shaped rectangular specimens with a total length of 38 mm, a gauge cross-section of 3.0 mm × 2.0 mm, and a gauge length of 12 mm were prepared from the as-prepared sheets using wire electrical discharge machining (EDM). Before tensile testing, the surfaces of the tensile specimens were ground using 2000 grit SiC paper. A 10 mm extensometer was utilized to measure the engineering strain within the gauge section. Tensile tests were performed at ambient temperature with a 10 kN SANS CMT4104 testing machine at an engineering strain rate of 1.0×10^{-3} s^{-1}. Three tensile specimens were tested to check reproducibility. The tensile direction was parallel to rolling direction (RD) of rolled plate.

To evaluate the fracture toughness, CT specimens with various thicknesses ranging from $B = 2.5$ to 30 mm and widths ranging from $W = 20$ to 60 mm were cut from the sheet of CP-Ti and LO-Ti. Nonlinear elastic-fracture mechanics in accordance with ASTM Standard E1820 was used to evaluate the fracture toughness of CP-Ti and LO-Ti.[35] Three CT specimens of each thickness were tested to check reproducibility. More details on the fracture toughness testing are described in the Supplementary Text (Supporting Information).

Standard subsize Charpy 45° V-notch specimens with a size of 10 × 10 × 55 mm^3 were used in Charpy impact tests, in accordance with ASTM Standard E23.[36] The depth of notch and the diameter at the base of the notch were ≈2 mm and ≈0.25 mm, respectively. The impact experiments for CP-Ti and LO-Ti were performed using a 450-J-capacility MTS impact testing machine. To ensure repeatability, at least three samples were tested for each material.

Microstructural Characterizations: To visually survey the crack propagation ability in different samples, and to discern the deformation mechanisms near the crack tip under plane–stress conditions, the in situ crack propagation processes were captured and monitored on the surfaces of CP-Ti and LO-Ti CT samples ($B = 5$ mm, $W = 20$ mm) using a video camera (see Movies S1 and S2 in the Supporting Information). Before testing, both CP-Ti and LO-Ti CT samples were ground and mechanically polished to achieve a surface roughness of 0.05 µm. The deformed morphologies present on the surface near the crack tip and crack wake were characterized using a SEM (Hitachi SU6600) operating in secondary electron (SE) imaging mode at 15 kV.

To clarify the toughening mechanisms under plane–strain conditions, some CT samples with a thickness of $B = 10$ mm and side grooves were sliced through the thickness into two halves at the midsection thickness after fracture toughness testing. The interior surface of one half was imaged using SE and backscattered electron (BSE) imaging modes in Hitachi SU6600 SEM operating at 15 kV. To reveal further details on the sample surface, an electrochemical polishing was employed using a solution consisting of 10 vol% perchloric acid and 90 vol% methanol at a voltage of 30 V and a temperature of −50 °C for 30 s. Following this treatment, EBSD scans were conducted near the crack tip at the midplane of CP-Ti and LO-Ti CT samples using the Zeiss Gemini 500 SEM operated at 15 kV with a step size of 0.15–0.6 µm. The KAM maps with a kernel size of 5 × 5 and a maximum angle of 5° were generated considering the first-nearest neighbors of each measured point using AZtecCrystal software: https://nano.oxinst.com/azteccrystal. The GND density maps, corresponding to ⟨*a*⟩ and ⟨*c*+*a*⟩ dislocations, identified by their respective Burgers vectors, were also generated. To reveal the deformed morphologies near the crack tip and wake under plane–strain conditions, polished samples were further etched for 20 s at ambient temperature using a mixture of 2 vol% hydrofluoric acid, 5 vol% nitric acid, and 43 vol% distilled water. SE and BSE imaging modes were used to characterize the twinning morphologies on featured regions along the crack propagation direction. The initial microstructures of CP-Ti and ULO-Ti samples were also characterized using EBSD (Zeiss Gemini 500) after electropolishing. The average grain sizes were measured by a line intercept method.

TEM was used to investigate the twinning and dislocation substructure near the crack tip of the CP-Ti and LO-Ti CT samples. TEM observations were performed in an FEG JEOL 2100F high-resolution TEM at 200 kV with a double tilt holder. To examine the dislocation structure present under plane–strain conditions ahead of the crack tip, CT specimens with a crack extension of $\Delta a \approx 2.5$ mm were used to cut thin foils at the midplane using EDM, and then mechanically ground down to about 50 µm. Disks of 3 mm in diameter containing the crack tip were punched and dimpled in the center, followed by twin-jet electrochemical polishing under an operation voltage of 30 V at −50°. The polishing electrolyte was a mixture of 10 vol% perchloric acid and 90 vol% methanol. To prepare TEM specimens, the region at the crack front was first thinned down to about 30 µm using a dimpling grinder (Model 200), and then the crack region was covered with two pieces of thin foil to prevent light transmission and damage to the crack tip by the electrolyte during subsequent electropolishing. Finally, thin regions inside the plastic zone of CP-Ti and LO-Ti were obtained, as illustrated in Figure S12a,c,d (Supporting Information). It is worth noting that the thinning process did not introduce any new deformation, as evidenced by a comparison of the initial samples before and after dimpling. Therefore, the postmortem TEM analysis conducted at room temperature did not further alter the morphologies of dislocations/twinning, and should be considered as an accurate representation of their original state. Standard **g**•**b** analysis (where **g** is the diffraction vector and **b** is the Burgers vector of dislocations) was conducted under a two-beam condition from the $[11\bar{2}0]$ zone axis.

Statistical Analysis: Tensile properties including the yield strength (σ_y), the ultimate tensile strength (σ_{uts}), and the elongation to fracture (ε_f) were determined from the tensile engineering stress–strain curves. True stress–strain curves and strain hardening rate curves were also calculated to extract the uniform elongation and the work of fracture, $u_f = \int_0^{\varepsilon_{f,p}} \sigma d\varepsilon_p$, during tensile fracture, which was determined from the area under true stress–plastic strain curve, where $\varepsilon_{f,p}$ is the plastic strain corresponding to the elongation to failure, ε_f. Average values and standard deviations of these tensile properties are summarized in Table S2 (Supporting Information). Mean and standard deviations of fracture toughness were calculated from three CT specimens at each sample thickness and are displayed in Table S2 (Supporting Information). Three standard subsize Charpy 45° V-notch specimens were used to determine the mean and standard deviations of impact energy for CP-Ti and LO-Ti.

Supporting Information

Supporting Information is available from the Wiley Online Library or from the author.

Acknowledgements

W.-Z.H. gratefully acknowledges funding from the National Natural Science Foundation of China (Grant Nos. 51922082 and 51971170). E.M. acknowledges XJTU for hosting his work at CAID. X.-W.Z. acknowledges Z. J. Ren of Instrument Analysis Center of Xi'an Jiaotong University for assistance with EBSD analysis.

Conflict of Interest

The authors declare no conflict of interest.

Author Contributions

W.-Z.H. conceived the project and supervised the research. W.-Z.H. and E.M. led the writing of the paper. X.-W.Z. performed the mechanical tests and microstructural characterizations under the guidance of W.-Z.H. All authors analyzed the data and contributed to discussions.

Data Availability Statement

The data that support the findings of this study are available from the corresponding author upon reasonable request.

Keywords

⟨*c*+*a*⟩ slip, fracture toughness, oxygen, titanium, twinning

Received: June 11, 2024
Revised: August 14, 2024
Published online: August 26, 2024

[1] K. Lu, *Science* **2010**, *328*, 319.
[2] N. E. Paton, J. C. Williams, G. P. Rauscher, in *Titanium Science and Technology, Metallurgical Society of AIME*, vol. *2*, Plenum Press, New York, NY **1973**, pp. 1049–1069.
[3] P. A. Russo, S. R. Seagle, *ASTM Spec. Tech. Publ.* **1984**, *830*, 99.
[4] Q. Yu, L. Qi, T. Tsuru, R. Traylor, D. Rugg, J. W. Morris, M. Asta, D. C. Chrzan, A. M. Minor, *Science* **2015**, *347*, 635.
[5] S. Zhao, R. Zhang, Q. Yu, J. Ell, R. O. Ritchie, A. M. Minor, *Science* **2021**, *373*, 1363.
[6] Y. M. Zhu, K. Zhang, Z. C. Meng, K. Zhang, P. Hodgson, N. Birbilis, M. Weyland, H. L. Fraser, S. C. V. Lim, H. Z. Peng, R. Yang, H. Wang, A. J. Huang, *Nat. Mater.* **2022**, *21*, 1258.
[7] T. T. Song, Z. B. Chen, X. Y. Cui, S. L. Lu, H. S. Chen, H. Wang, T. Dong, B. L. Qin, K. C. Chan, M. Brandt, X. Z. Liao, S. P. Ringer, M. Qian, *Nature* **2023**, *618*, 63.
[8] M. F. Ashby, in *Materials Selection in Mechanical Design* (Ed: M. F. Ashby), 4th ed., Butterworth-Heinemann, Oxford **2011**, pp. 31–56.
[9] Y. P. Zheng, W. D. Zeng, D. Li, Q. Y. Zhao, X. B. Liang, J. W. Zhang, X. Ma, *J. AlloysCompd.* **2017**, *709*, 511.
[10] P. Guo, Y. Q. Zhao, W. D. Zeng, Q. Hong, *Mater. Sci. Eng., A* **2013**, *563*, 106.
[11] A. Gutierrez, M. Hahn, Y. J. Li, A. Dehbozorgi, W. Hohorst, M. Schwartz, J. Orlita, Y. T. Hein, N. Guanzon, X. D. Sun, O. S. Es-Said, *J. Mater. Eng. Perform.* **2019**, *28*, 7155.
[12] B. Gludovatz, A. Hohenwarter, D. Catoor, E. H. Chang, E. P. George, R. O. Ritchie, *Science* **2014**, *345*, 1153.
[13] B. Gludovatz, A. Hohenwarter, K. V. S. Thurston, H. B. Bei, Z. G. Wu, E. P. George, R. O. Ritchie, *Nat. Commun.* **2016**, *7*, 10602.
[14] D. Liu, Q. Yu, S. Kabra, M. Jiang, P. Forna-Kreutzer, R. P. Zhang, M. Payne, F. Walsh, B. Gludovatz, M. Asta, A. M. Minor, E. P. George, R. O. Ritchie, *Science* **2022**, *378*, 978.
[15] A. Hilhorst, P. J. Jacques, T. Pardoen, *Acta Mater.* **2023**, *260*, 119280.
[16] X. R. Liu, F. Hao, J. Wang, X. F. Chen, P. Jiang, F. P. Yuan, H. B. Li, E. Ma, X. L. Wu, *J. Mater. Sci. Technol.* **2022**, *108*, 256.
[17] R. O. Ritchie, *Nat. Mater.* **2011**, *10*, 817.
[18] L. Liu, Q. Yu, Z. Wang, J. Ell, M. X. Huang, R. O. Ritchie, *Science* **2020**, *368*, 1347.
[19] B. A. Bilby, A. G. Crocker, *Proc. R. Soc. Lond. A* **1965**, *288*, 240.
[20] P. G. Partridge, *Metall. Rev.* **1967**, *12*, 169.
[21] S. G. Song, G. T. Gray, *Acta Metall. Mater.* **1995**, *43*, 2339.
[22] Z. X. Wu, W. A. Curtin, *Nature* **2015**, *526*, 62.
[23] Z. X. Wu, W. A. Curtin, *Proc. Natl. Acad. Sci. USA* **2016**, *113*, 11137.
[24] H. Li, D. E. Mason, T. R. Bieler, C. J. Boehlert, M. A. Crimp, *Acta Mater.* **2013**, *61*, 7555.
[25] M. A. Kumar, I. J. Beyerlein, C. N. Tome, *Acta Mater.* **2016**, *116*, 143.
[26] Z. X. Wu, R. Ahmad, B. L. Yin, S. Sandlöbes, W. A. Curtin, *Science* **2018**, *359*, 447.
[27] B. Y. Liu, F. Liu, N. Yang, X. B. Zhai, L. Zhang, Y. Yang, B. Li, J. Li, E. Ma, J. F. Nie, Z. W. Shan, *Science* **2019**, *365*, 73.
[28] M. S. Hooshmand, C. Niu, D. R. Trinkle, M. Ghazisaeidi, *Acta Mater.* **2018**, *156*, 11.
[29] Y. Chong, M. Poschmann, R. P. Zhang, S. T. Zhao, M. S. Hooshmand, E. Rothchild, D. L. Olmsted, J. W. Morris, D. C. Chrzan, M. Asta, A. M. Minor, *Sci. Adv.* **2020**, *6*, eabc4060.
[30] Y. Chong, R. P. Zhang, M. S. Hooshmand, S. T. Zhao, D. C. Chrzan, M. Asta, J. W. Morris, A. M. Minor, *Nat. Commun.* **2021**, *12*, 6158.
[31] Y. Chong, R. Gholizadeh, T. Tsuru, R. P. Zhang, K. Inoue, W. Q. Gao, A. Godfrey, M. Mitsuhara, J. W. Morris, A. M. Minor, N. Tsuji, *Nat. Commun.* **2023**, *14*, 404.
[32] X. Q. Wang, W. Z. Han, *Acta Mater.* **2023**, *246*, 118674.
[33] X. Li, *Nat. Mater.* **2023**, *22*, 402.
[34] S. X. Huang, Q. Y. Zhao, C. Lin, C. Wu, Y. Q. Zhao, W. J. Jia, C. L. Mao, *Mater. Sci. Eng., A* **2021**, *818*, 141394.
[35] ASTM International, *E1820-20 Standard Test Method for Measurement of Fracture Toughness*, ASTM International, West Conshohocken, PA, USA, **2020**.
[36] ASTM International, E23-20 Standard Test Method for Notched Bar Impact Testing of Metallic Materials, ASTM International, West Conshohocken, PA, USA, **2020**.
[37] W. J. Mills, *J. Test. Eval.* **1981**, *9*, 56.
[38] B. Cotterell, J. Rice, *Int. J. Fract.* **1980**, *16*, 155.
[39] A. S. Ayman, R. K. Surya, D. D. Roger, *Acta Mater.* **2003**, *51*, 4225.
[40] Y. Minonishi, S. Morozumi, H. Yoshinaga, *Scr. Metall.* **1982**, *16*, 427.
[41] H. Numakura, Y. Minonishi, M. Koiwa, *Scr. Metall.* **1986**, *20*, 1581.
[42] Y. Lu, Y. H. Zhang, E. Ma, W. Z. Han, *Proc. Natl. Acad. Sci. USA* **2021**, *118*, 21105961182021.
[43] J. W. Zhang, J. X. Wang, X. W. Zou, I. J. Beyerlein, W. Z. Han, *Acta Mater.* **2022**, *234*, 118023.
[44] M. Y. Gong, S. Xu, D. Y. Xie, S. J. Wang, J. Wang, C. Schuman, J. S. Lecomte, *Acta Mater.* **2019**, *164*, 776.
[45] X. H. Lin, W. Z. Han, *Acta Mater.* **2024**, *269*, 119825.
[46] D. R. Steinmetz, T. Jäpel, B. Wietbrock, P. Eisenlohr, I. Gutierrez-Urrutia, A. Saeed-Akbari, T. Hickel, F. Roters, D. Raabe, *Acta Mater.* **2013**, *61*, 494.
[47] Y. Deng, C. C. Tasan, K. G. Pradeep, H. Springer, A. Kostka, D. Raabe, *Acta Mater.* **2015**, *94*, 124.